



**HAL**  
open science

## Joint measurement of the atmospheric muon flux through the Puy de Dôme volcano with plastic scintillators and Resistive Plate Chambers detectors

F. Ambrosino, A. Anastasio, A. Bross, S. Béné, P. Boivin, L. Bonechi, C. Cârloganu, R. Ciaranfi, L. Cimmino, C. Combaret, et al.

### ► To cite this version:

F. Ambrosino, A. Anastasio, A. Bross, S. Béné, P. Boivin, et al.. Joint measurement of the atmospheric muon flux through the Puy de Dôme volcano with plastic scintillators and Resistive Plate Chambers detectors. *Journal of Geophysical Research: Solid Earth*, 2015, 120, pp.7290-7307. 10.1002/2015JB011969 . in2p3-01270741

**HAL Id: in2p3-01270741**

**<https://hal.in2p3.fr/in2p3-01270741>**

Submitted on 1 Jun 2021

**HAL** is a multi-disciplinary open access archive for the deposit and dissemination of scientific research documents, whether they are published or not. The documents may come from teaching and research institutions in France or abroad, or from public or private research centers.

L'archive ouverte pluridisciplinaire **HAL**, est destinée au dépôt et à la diffusion de documents scientifiques de niveau recherche, publiés ou non, émanant des établissements d'enseignement et de recherche français ou étrangers, des laboratoires publics ou privés.

**1 Joint measurement of the atmospheric muon flux**  
**2 through the Puy de Dôme volcano with plastic**  
**3 scintillators and Resistive Plate Chambers detectors**

F. Ambrosino,<sup>1,2</sup> A. Anastasio,<sup>2</sup> A. Bross,<sup>3</sup> S. Béné,<sup>4</sup> P. Boivin,<sup>5</sup> L. Bonechi,<sup>6</sup>  
C. Cârloganu,<sup>4</sup> R. Ciaranfi,<sup>7</sup> L. Cimmino,<sup>1,2</sup> Ch. Combaret,<sup>8</sup> R.  
D'Alessandro,<sup>6,7</sup> S. Durand,<sup>9</sup> F. Fehr,<sup>4</sup> V. Français,<sup>4</sup> F. Garufi,<sup>1,2</sup> L. Gailler,<sup>5</sup>  
Ph. Labazuy,<sup>5</sup> I. Laktineh,<sup>8</sup> J-F Lénat,<sup>5</sup> V. Masone,<sup>2</sup> D. Miallier,<sup>4</sup> L.  
Mirabito,<sup>8</sup> L. Morel,<sup>9</sup> N. Mori,<sup>6,7</sup> V. Niess,<sup>4</sup> P. Noli,<sup>2</sup> A. Pla-Dalmau,<sup>3</sup> A.  
Portal,<sup>5</sup> P. Rubinov,<sup>3</sup> G. Saracino,<sup>1,2</sup> E. Scarlini,<sup>6,7</sup> P. Strolin,<sup>1,2</sup> B. Vulpescu<sup>4</sup>

---

Corresponding author: C. Cârloganu (Cristina.Carloganu@in2p3.fr), P. Noli (noli@na.infn.it)

<sup>1</sup>Dipartimento di Fisica, Università degli

D R A F T

August 31, 2015, 5:01pm

D R A F T

4 **Abstract.** The muographic imaging of volcanoes relies on the measured  
5 transmittance of the atmospheric-muon flux through the target. An impor-  
6 tant bias affecting the result comes from background contamination mim-  
7 icking a higher transmittance. The MU-RAY and TOMUVOL collaborations  
8 measured independently in 2013 the atmospheric muon flux transmitted through  
9 the Puy de Dôme volcano using their early prototype detectors, based on plas-  
10 tic scintillators and on Glass Resistive Plate Chambers, respectively. These  
11 detectors had three (MU-RAY) or four (TOMUVOL) detection layers of  $1 \text{ m}^2$   
12 each, tens (MU-RAY) or hundreds (TOMUVOL) of ns time resolution, a few  
13 mm position resolution, an energy threshold of few hundreds MeV and no  
14 particle identification capabilities. The prototypes were deployed about 1.3 km  
15 away from the summit, where they measured, behind rock depths larger than  
16 1000 m, remnant fluxes of  
17  $1.83 \pm 0.50(\text{syst}) \pm 0.07(\text{stat}) \text{ m}^{-2} \text{ day}^{-1} \text{ deg}^{-2}$  (MU-RAY) and  $1.95 \pm 0.16(\text{syst}) \pm 0.05(\text{stat}) \text{ m}^{-2} \text{ day}^{-1} \text{ deg}^{-2}$   
18 (TOMUVOL), that roughly correspond to the expected flux of high-energy  
19 atmospheric muons crossing 600 metres water equivalent (m.w.e) at  $18^\circ$  el-  
20 evation. This implies that imaging depths larger than 500 m.w.e from 1 km  
21 away using such prototype detectors suffers from an overwhelming background.  
22 These measurements confirm that a new generation of detectors with higher  
23 momentum threshold, time-of-flight measurement and/or particle identifi-  
24 cation is needed. The MU-RAY and TOMUVOL collaborations expect shortly

---

Studi di Napoli Federico II, Italy.

25 to operate improved detectors, suitable for a robust muographic-imaging of  
26 kilometre scale volcanoes.

---

<sup>2</sup>INFN, Napoli, Italy.

## 1. Muon imaging of volcanoes

---

<sup>3</sup>Fermilab PO Box 500 Batavia IL  
60510-5011

<sup>4</sup>Clermont Université, Université Blaise  
Pascal, CNRS/IN2P3, Laboratoire de  
Physique Corpusculaire, BP 10118, F-63000  
Clermont-Ferrand, France.

<sup>5</sup>Laboratoire Magmas et Volcans,  
Université Blaise Pascal - CNRS - IRD,  
OPGC, 5 rue Kessler, 63038 Clermont  
Ferrand, France.

<sup>6</sup>Dipartimento di Fisica, Università degli  
Studi di Firenze, Italy.

<sup>7</sup>INFN, Firenze, Italy.

<sup>8</sup>Université de Lyon, Université Lyon 1,  
CNRS/IN2P3, IPNL, 1 Rue E. Fermi, 69622  
Villeurbanne Cedex, France.

<sup>9</sup>Ecole Supérieure des Géomètres et  
Topographes du Mans, France.

27 Volcanic hazard assesment and risk mitigation remain two very important scientific  
28 subjects with heavy implications both on the population safety and economic develop-  
29 ment [*Brown et al.*, 2015]. Anticipating future activity of volcanoes requires monitoring  
30 of their activity as well as information on their past behaviour and their internal struc-  
31 ture. Monitoring volcano activity, that may be regarded as dynamic imaging of changes  
32 occurring inside and below the edifices, routinely uses a large number of methods (see for  
33 example [*Smith*, 2009]). Structural geophysical studies, that may be considered as static  
34 imaging, aim at identifying and characterising the architecture of the edifices, their plumb-  
35 ing systems, as well as the mechanical characteristics of the rocks. They are inferred from  
36 the internal distribution of various physical quantities such as electrical resistivity [*Revil*,  
37 2008], density [*Li*, 1998; *Gailler*, 2009], magnetisation [*Gailler*, 2012], or seismic veloc-  
38 ity [*Lees*, 2007]).

39 The plumbing system comprises magma reservoirs and conduits. Magma reservoirs are  
40 usually located at depths ranging from few to tens of kilometres and therefore may be  
41 detected only by techniques with a large depth of investigation. The conduits connect  
42 magma reservoirs to the surface. More superficial than the reservoirs, their size is also  
43 smaller than typical reservoir sizes, which may increase the detection difficulty. Typical  
44 sizes vary from metres in case of the mafic dikes to hundreds of metres for the chimney  
45 of more felsic magmas. The architecture of the edifices is important to know because  
46 it will not only influence the magma paths (the conduits), but it may also generate its  
47 own volcano-tectonic activity through gravitational instabilities [*Mc Guire*, 1996]. For  
48 example, zones of an edifice weakened by hydrothermal alteration will be prone to slide  
49 as huge flank landslides [*Siebert*, 1987; *Lopez and Williams*, 1993].

50 The need of high resolution imaging of the interior of the volcanic edifices is there-  
51 fore well justified and is a main motivation for developping and refining the geophysical  
52 methods currently employed in volcanology.

53 Recently, radiography with atmospheric muons [*Alvarez*, 1970; *Nagamine*, 1995], re-  
54 ferred to as muography in the following, was made possible by the development of reason-  
55 ably priced, large area, high efficiency and high precision muon trackers. Several groups  
56 ([*Tanaka*, 2007, 2010, 2011; *Marteau*, 2012; *Lesparre*, 2012; *Fehr*, 2012; *Portal*, 2013;  
57 *Tanaka*, 2014]) have already applied this method for the exploration of volcanic edifices  
58 of moderate size.

59 The basic idea behind volcano muography is that measuring the absorption of the atmo-  
60 spheric muon flux as a function of the direction at a fixed location allows mapping out the  
61 average column density in the volcano after accounting for the topography. By repeating  
62 the measurement from different locations, three-dimensional models of the matter density  
63 distribution can be inferred.

64 Muography offers some clear advantages over traditional geophysical methods in terms  
65 of attainable resolution and ease of installation and deployment since the measurement  
66 can be performed remotely from the risk area whereas most other geophysical methods  
67 require to make measurements on the field above the active areas. The muography suffers  
68 though from the fact that the high energy muons that can cross large edifices are rare.  
69 This has a direct implication on the size of the detectors that need to be deployed in order  
70 to measure a sizeable number of events in a reasonable time. It also requires a very tight  
71 control of the background affecting the measurements, be it physical or detector induced.

72 In this contribution, we describe a new muography experiment on a complex volcanic  
73 edifice, a compound lava dome. Lava domes are volcanic edifices created both by magma  
74 intrusion into the dome interior (endogenous growth) and by extrusion of spines, lobes  
75 or short lava flows (exogenous growth). Dome magmas are too viscous to flow over  
76 significant distances and will accumulate above and near the vent. Domes exhibit a large  
77 range of shapes and sizes, depending on their construction history. Their surface is often  
78 constituted by rock fragments forming a talus on the sides. Inside, cores of solidified  
79 magma are present. Domes seldom form during a single episode. Most of the time  
80 successive episodes of dome growth occur during an eruption of highly variable duration,  
81 that can last weeks or years. Collapse of parts of the dome may be accompanied by  
82 explosions and pyroclastic flows. The compound lava dome formed by the end of the  
83 eruption includes volcanic ash and pyroclastites intermixed with rock fragments derived  
84 from solidified lava and massive intrusions and extrusions. Its flank will be composed of  
85 unstable rock debris.

86 Such complex formations of compound lava domes have been well documented in re-  
87 cent eruptions of Mount Saint Helens [*Major*, 2009; *Vallance*, 2010; *Swanson*, 1987], Un-  
88 zen [*Nakada*, 1993, 1995, 1999], Montserrat [*Calder*, 2002; *Ryan*, 2010; *Watts*, 2002] or  
89 Santiaguito [*Bluth*, 2004; *Harris*, 2003; *Rose*, 1972]. When the formation of a compound  
90 dome has not been witnessed or monitored, its history and internal structure are more  
91 difficult to establish. They will rely on geological analysis of the products at the surface  
92 and on structural geophysical studies. Moreover, even in the case of compound lava domes  
93 monitored during growth, the internal structure may be poorly known since internal pro-  
94 cesses as endogenous growth or hydrothermal activity cannot be observed directly.



95 The compound lava dome of the experiment is the Puy de Dôme, located in the Chaîne  
96 de Puys volcanic district in France. This  $\sim 11000$  years old edifice has an altitude of  
97 1465 m (a.s.l) and a lateral extension of more than 2 km at the base. Geological studies  
98 lead to a three-step model for the Puy de Dôme growth [*Boivin, 2009; Camus, 1975*]. A  
99 first cumulo-dome, emplaced on a cluster of several scoria cones and their associated lava  
100 flows, forms the western part of the volcano. After the partial destruction of the eastern  
101 part of this unit, a spiny extrusion grew into the collapse scar, forming the second unit.  
102 The eruption ended by a summit phreatic/phreatomagmatic event [*Miallier, 2010*]. The  
103 alteration observed on several summit outcrops indicates that the growth of Puy de Dôme  
104 was accompanied by a strong fumarolic and hydrothermal activity.

105 The Puy de Dôme is an interesting target for muon imaging. It is isolated and its  
106 basement at an altitude of about 950 m (a.s.l) greatly facilitates the deployment of muon  
107 detectors. The edifice size is moderate enough to expect that a large part may be in-  
108 vestigated with atmospheric muons. The recent geology survey [*Boivin, 2013*] and a  
109 preliminary geophysical survey [*Portal, 2013*] raise questions over the validity of the pre-  
110 vious model and suggest that the interior of the edifice is heterogeneous. This geological  
111 heterogeneity should be reflected in the density distribution.

112 This first attempt by the MU-RAY [*Ambrosino, 2014; Anastasio, 2013; Anastasio,*  
113 *bis, 2013; Ambrosi, 2011*] and TOMUVOL [*Cârloganu, 2013*] collaborations to measure  
114 through muography the transmittance of the inner structure of the Puy de Dôme was  
115 made in 2013.

116 The two detectors, described in detail in Section 2 and Section 3, are modular, robust  
117 and designed for low power consumption, despite a fine segmentation and three or four

118 tracking layers. They differ in the detection techniques and the two collaborations have  
119 used independent data acquisition and analysis strategies. They are both prototypes of  
120 more advanced detectors foreseen for the muography, that will have higher momentum  
121 thresholds and will include time-of-flight measurements.

122 Since muography is a new technique and the robustness of the density measurement ver-  
123 sus experimental and methodological biases was not assessed yet, we have chosen to treat  
124 the Puy de Dôme measurement reported here as two independent experiments performed  
125 with the two detectors, rather than a combined one. This approach is conservative and  
126 should lead to the identification of eventual detection biases, specific for each of the two  
127 detectors. Similarly, the methodological part (detector calibration, muon reconstruction  
128 and selection of the muon candidates used for inferring the target transmittance) is also  
129 independent and should allow us to infer the systematical biases affecting the muographic  
130 measurements from the difference between the MU-RAY and TOMUVOL results.

131 One of the major advantages of the muography being the capability of performing  
132 measurements from the outskirts of the risk areas, the two detectors were deployed about  
133 1.3 km away from the summit, at about the same altitude (1000 m a.s.l). The detection  
134 views were South-North for the MU-RAY detector and East-West for the TOMUVOL  
135 detector as it can be seen on the top picture of Figure 1. We use a detector-wise elevation  
136 ( $\alpha$ ) - azimuth ( $\beta$ ) coordinate system rotated about the vertical axis such that azimuth  
137 zero is the normal to the first detection layer pointing towards Puy de Dôme. It was  
138 checked that the detection layers were vertical with an accuracy better than 1 degree. In  
139 this right-handed coordinate system with the origin set in turn by each detector, the path

140 length that the atmospheric muons would have to travel through the volcano in order to  
141 reach the detectors is represented in the middle and bottom plots of Figure 1.

142 The path lengths were calculated from a high resolution digital elevation model re-  
143 binned using  $2.5 \times 2.5 \times 2.5$  m<sup>3</sup> bins.

144 Two regions in  $\alpha$  and  $\beta$  with path lengths in the 1.5 to 2 km range, called in the  
145 following “control regions”, are defined for each site. They are represented by black  
146 rectangles superimposed on the path length plots of Figure 1.

147 To estimate the number of expected muon events crossing the volcano in a given di-  
148 rection, the two collaborations use two different strategies. MU-RAY follows the method  
149 described in [Okubo, 2012]: first, the atmospheric muon flux (differential in energy and  
150 zenith angle), is evaluated using the Matsuno model as reported in [Matsuno, 1984]; then a  
151 transmission table giving the percentage of surviving muons as a function of the integrated  
152 density of rock to cross is calculated using the GEANT4 simulation toolkit [GEANT4,  
153 2003], in which the majority of the physics processes involving high energy muons are  
154 simulated; after estimating along each direction the rock thickness, the flux is convoluted  
155 with the transmission to infer the expected number of events for each direction.

156 TOMUVOL uses the differential spectrum of atmospheric muons from [Chirkin, 2004].  
157 In the model proposed therein, the altitude correction is implemented for the average  
158 track length of the muons and for the atmosphere mass overburden using the exponential  
159 atmospheric model, as cited in the paper. Neglecting the scattering, high energy muons  
160 are then assumed to follow straight-line trajectories from their generation point in the  
161 upper atmosphere down to sea level. The energy loss of muons in the matter crossed  
162 during their travel is computed with the Continuously Slowing Down Approximation

163 (CSDA) [*Groom*, 2001], using the tabulated values for “dry air” and “standard rock”  
164 (with a density renormalised to  $1.66 \text{ g/cm}^3$ ) as provided online by [*PDG*, 2014].

165 The value of  $1.66 \text{ g/cm}^3$  was suggested by density measurements of about 100 rock sam-  
166 ples collected on various parts of the Puy de Dôme. The sample densities range between  
167  $1.2$  and  $2.15 \text{ g/cm}^3$ . It is unlikely that densities significantly higher than  $2.15 \text{ g/cm}^3$  exist  
168 in the bulk of the dome because the measured samples should represent all the known  
169 structural units of the volcano. Actually, the batch mean-value is  $1.88 \text{ g/cm}^3$ , but the  
170 relative contributions of the different petrographic facies in the batch are certainly not  
171 the same as for the whole edifice. Moreover, the mean density at a multi-metric scale  
172 should account for voids between rocky materials, for example within cracks or loose de-  
173 posits. Also, the Nettleton test on the gravimetry measurements [*Portal*, 2013] finds that  
174 the Bouguer anomalies are least correlated with the altitude when assuming an average  
175 density of the dome of  $1.8 \text{ g/cm}^3$ . Let us stress though that the average density of the  
176 dome is used here just for having a first order estimate of the expected number of muons  
177 crossing the volcano. The actual density measurement (Section 4) does not require a first  
178 guess of the volcano average bulk density as in the case of the gravimetric tomography.  
179 The ballistic muons crossing the volcano along a given direction are independent of the  
180 ballistic muons crossing along other directions and thus are the measurements of the in-  
181 tegrated densities along different directions, provided that the flux of atmospheric muons  
182 is correctly accounted for.

183 The TOMUVOL approach was used to estimate the number of muons originating from  
184 the control regions defined in Figure 1, that should be recorded with an ideal detector  
185 of size  $1 \text{ m} \times 1 \text{ m} \times 1 \text{ m}$ , when located in turn at the two deployment sites and pointing

186 towards ( $\alpha = 0, \beta = 0$ ). The expected statistics after one month of data taking is shown  
187 in Figure 2. The muon rate is estimated to be  $30 \mu\text{Hz}$  for the MU-RAY deployment site  
188 and  $14 \mu\text{Hz}$  for the TOMUVOL site. The MU-RAY approach leads to an estimate of  
189  $56 \mu\text{Hz}$  for the MU-RAY site. Although the expected rates using the two approaches  
190 differ by nearly a factor two, this (as will be shown in section 4) pales into insignificance  
191 when compared to the actual measured rates.

192 For completeness sake, let us quote also the muon rates in an ideal,  $1 \text{ m} \times 1 \text{ m} \times 1 \text{ m}$   
193 detector located at the MU-RAY site, following the MU-RAY approach and assuming  
194 extreme densities of 1 and  $2.5 \text{ g/cm}^3$ . They are of  $267 \mu\text{Hz}$  and  $10 \mu\text{Hz}$  respectively.

195 In fact, for realistic densities, it is obvious that in the control regions at the very base of  
196 the Puy de Dôme, there is a small expectation of detecting high energy muons crossing the  
197 volcano with a  $1 \text{ m} \times 1 \text{ m} \times 1 \text{ m}$  detector during one month of data taking. These regions  
198 can therefore be used as control regions for the background affecting the measurement.  
199 It should be stated that the regions are shifted by  $4^\circ$  from the horizontal, since none of  
200 the two detectors had for this campaign a time-of-flight measurement; both are therefore  
201 unable to discriminate between the tracks arriving from the volcano side and from the  
202 opposite side when the tracks are nearly horizontal. However, as it will be seen in the  
203 following sections, the angular resolutions of both detectors are good enough that above  
204  $\alpha \sim 4^\circ$  the residual contamination with tracks from the opposite direction should be  
205 negligible. Technical developments are underway within both collaborations and in the  
206 future both detectors are expected to have a time-of-flight measurement.

207 After reporting on the measurements of the muon flux in the free sky and through the  
208 Puy de Dôme performed independently by the MU-RAY and TOMUVOL collaborations

209 in Section 4, the implication on the muography of kilometre scale volcanoes is discussed  
210 in Section 5.

## 2. The MU-RAY detector

211 The MU-RAY telescope [*Anastasio, 2013*] is based on plastic scintillators. Each scin-  
212 tillator bar has a triangular cross-section, with a base of 3.3 cm, a height of 1.7 cm and  
213 a length of 107 cm. The bars, produced at FERMILAB-NICADD [*Pla-Dalmau, 1999*],  
214 are extruded and coated with a  $\text{TiO}_2$  layer 0.25 mm thick to increase the light yield. A  
215 hole along the bar axis hosts a Wave Length Shifting (WLS) fibre. A module of 32 bars  
216 grouped together is 0.5 m wide and weighs less than 20 kg. The 32 fibres are routed  
217 to a specifically designed fibre connector that is coupled to a custom designed Printed  
218 Circuit Board (PCB). The PCB board hosts 32 silicon photomultipliers (SiPMs), custom  
219 designed by FBK-IRST [*Piazza, 2010*].

220 When a muon crosses a scintillator bar, light is produced. The WLS fibres collect  
221 and carry the light to the SiPMs, which convert the light pulse into an electric signal,  
222 processed by the front end electronics (Slave board). The Slave outputs a fast digital  
223 signal whenever one or more SiPM produce a signal above a programmable threshold  
224 (local trigger). The local trigger is carried to a control board (Master), which collects  
225 all the local triggers that have been sent from the Slave modules and produces a global  
226 trigger signal according to a programmable trigger logic. The charge produced by each  
227 SiPM is proportional to the energy released by the muon in the scintillator bar and is  
228 converted by an Analog to Digital Converter (ADC) and acquired by the Master board.

229 Two modules, assembled side by side, form an  $X$  or  $Y$  layer of about  $1 \text{ m}^2$  area, giving  
230 one of the two “cartesian” coordinates of the impact point of the muon on the layer. Two

231 layers with orthogonal bars form an  $X$ - $Y$  plane. The telescope consists of three  $X$ - $Y$  layers,  
232 mounted on an aluminium alloy frame. The frame can be rotated in the azimuthal plane,  
233 to acquire data with the telescope pointing to different regions of the sky for calibration  
234 purposes. The muon trajectory is reconstructed by a linear fit of the  $X$ - $Y$ - $Z$  points given  
235 by the three layers.

236 The SiPMs have a very low power consumption, are robust and compact. Their main  
237 drawback is the temperature dependence of the operating voltage and the high dark  
238 rates (compared to conventional phototubes), due to the thermally produced electron-  
239 hole pairs. In order to maintain the temperature under control, the SiPMs are thermally  
240 coupled through their PCB carrier to an external source kept at constant temperature.  
241 The specially developed water cooling system gives a temperature stability better than  
242  $0.1^{\circ}\text{C}$ .

243 The dark rates of the SiPMs used for the measurement presented here were as high as 1-  
244 2 MHz, though SiPMs with a lower dark rate are foreseen in the future. The discriminator  
245 threshold of the Slave was set such as to have, on average, a trigger rate of less than 2 kHz  
246 per SiPM, equivalent to about a 100 kHz rate per single view ( $X$  or  $Y$ ) . The local trigger  
247 signal has a width of 40 ns. The trigger logic is the coincidence of the six single view planes.  
248 The expected rate of random coincidences and the rate measured in the laboratory (less  
249 than 1 event per day) are far below the expected muon rate.

250 When a global trigger is produced, the Master board starts the data acquisition (DAQ)  
251 from the 12 Slaves. The maximum DAQ rate is 20 Hz. During the measurement campaign  
252 the measured trigger rate was of the order of few Hz and the typical correction for the  
253 dead time of the order of 20%.

254 An iron shield of 1 m<sup>2</sup> area and 3 cm thickness was installed between the first and the  
255 second  $X$ - $Y$  plane along the muon direction to stop muons with energy below 70 MeV and  
256 part of the cosmic soft component, i.e. electrons and positrons.

### 2.1. The Puy de Dôme measurement campaign

257 The MU-RAY detector has been deployed on the Puy de Dôme from beginning of June  
258 2013 to the beginning of December 2013. Data recording was discontinued from July  
259 22 till September 5 because of a storm, that damaged the commercial internet network  
260 for the remote control of the telescope. Apart from this, recording was successful for a  
261 total of 105 days. The first 4 and the last 9 days were devoted to calibration runs, with  
262 the telescope pointing towards the free sky. Data recording with the telescope pointing  
263 towards the Puy de Dôme lasted 92 days in total.

264 Each single data recording run consisted of  $10^4$  triggers and on average lasted about  
265 45 minutes. Before each run,  $10^4$  pedestal events were acquired. The local trigger rates  
266 of each board, which are dominated by dark count rates, were also measured. All these  
267 activities reduce the effective time, devoted to the physics data run, to about 87% of the  
268 total run time. The trigger logic required a signal from at least one of the scintillator bars  
269 belonging to each of the six  $X$  or  $Y$  planes. A small percentage ( $\sim 0.1\%$ ) of the triggered  
270 events contained corrupted data and were discarded during data analysis.

271 During the data taking period the trigger rate was stable, with an average value of  
272  $3.59 \pm 0.29$  Hz.

### 2.2. Data reconstruction and analysis



273 The data analysis starts with the reconstruction of the muon tracks event by event. The  
274 track reconstruction is performed independently in the  $X$ - $Z$  and  $Y$ - $Z$  projections, where  
275  $X$ ,  $Y$  and  $Z$  respectively give the horizontal, vertical and longitudinal coordinates.

276 A normalised energy is associated to each strip, defined as the ratio of the difference  
277 between the recorded ADC value and the mean pedestal value, respect to the r.m.s value of  
278 the pedestal distribution. Strip clusters are formed by grouping one or more neighbouring  
279 strips with a normalised energy greater than 5. To each cluster is associated a normalised  
280 energy and a position defined respectively as the sum of the strips energies and as the  
281 energy weighted average of the strips coordinates. Therefore the clusters give the  $X$ - $Z$  or  
282  $Y$ - $Z$  coordinates of a muon or any other particle that released enough energy in the strips.

283 Each cluster in the first plane is associated with a cluster in the third plane and the  
284 intersection of the straight line connecting the two clusters with the middle plane is  
285 evaluated. If a cluster is found in its neighbourhood, a linear fit of the three clusters is  
286 performed and, if the fit converges, a candidate track in a single view is defined.

287 The procedure is repeated for all cluster combinations and produces a list of candidate  
288 tracks in both the  $X$ - $Z$  and  $Y$ - $Z$  projections. For each projection, the track candidate  
289 with the highest value of the minimum cluster energy is defined as the best candidate  
290 track. The three dimensional best candidate track is given by the two best candidate  
291 tracks in the two projections. In this procedure all the cuts are loose enough to ensure a  
292 high reconstruction efficiency. 92% of the events have at least one candidate track in each  
293 view.

294 To increase the quality of the tracks some further cuts are introduced (quality cut). The  
 295  $\chi^2/n.d.f.$  of the fit must be less than 5 and the minimum energy of the cluster associated  
 296 to the track must be greater than 20.

297 The maximum  $\chi^2/n.d.f.$  value and the minimum energy of the cluster were obtained  
 298 from a multi-parameter minimisation of the Punzi estimator [Punzi, 2003]. The proce-  
 299 dure maximises the efficiency of the selection for the muons sample while minimising the  
 300 acceptance for random triggers.

301 In this sample we select events containing just a single muon track (golden tracks) by  
 302 using an isolation cut. This cut is intended to reject events with tracks generated by the  
 303 soft component of the cosmic ray. The soft component can produce a shower hitting the  
 304 detector, generating more than one track or one track and one or more physical clusters.  
 305 The isolation cut requires that no cluster having a normalised energy greater than 20 and  
 306 not associated to the best candidate track is present in the event and that the number of  
 307 strips forming the clusters associated to the best track is less than 5. This golden tracks  
 308 sample has a track fit residual distribution with a standard deviation of  $\sim 4$  mm.

309 We define the selection efficiency  $\epsilon_{sel}(\alpha, \beta)$  as the number of events that satisfy, for each  
 310 view, the isolation cut divided by the number of events selected with the previous cuts.  
 311 In Figure 3  $\epsilon_{sel}(\alpha, \beta)$  is shown for both the forward and backward track directions. At  
 312 the end of this selection we estimate an average analysis efficiency  $\epsilon_{ana} = 47\%$ .

313 The golden track rate, of  $1.99 \pm 0.12$  Hz is shown in Figure 4 as a function of time.  
 314 The background rate, defined as the rate of tracks pointing towards the control region  
 315 defined in Section 1, was measured to be  $0.7 \pm 0.1$  mHz and is also represented as a  
 316 function of time by open red squares. It must be noticed that neither rates are correlated

317 to the temperature of the SiPMs though the local trigger rates are clearly correlated with  
318 their temperature. During the whole data taking period  $\sim 11.4 \times 10^6$  golden tracks were  
319 acquired. The ones pointing in the direction of Puy de Dôme are shown on Figure 5 as a  
320 function of the elevation angle  $\alpha$  and azimuth  $\beta$ .

321 The stripes that can be noticed in the Figure 5 are due to the discrete resolution of  
322 the detector. The impact position of a track is not continuous, but varies in steps being  
323 calculated from the position of the scintillators bars centres. As a consequence,  $\alpha$  and  $\beta$   
324 exhibit also discrete distributions.

### 3. The TOMUVOL detector

325 The TOMUVOL muon telescope is made of four parallel layers of gaseous trackers,  
326 Glass Resistive Plate Chambers (GRPCs) [*Bedjidian, 2011*] originating from research and  
327 development for the International Linear Collider detectors [*ILC, 2013*]. A single GRPC  
328 consists of two parallel thin glass plates kept 1.2 mm apart by tiny spacers so that gas (a  
329 mixture of TFE, SF6 and isobutane) can circulate between the plates. The outer sides of  
330 the glass plates are coated with a thin layer of resistive material on which high voltage is  
331 applied. Charged particles, passing through the chambers, ionise the gas and thus produce  
332 charge cascades, which in turn induce charge signals on 1 cm<sup>2</sup> copper cells etched on one  
333 face of a PCB placed on the anode glass. On the other face of the PCB are attached  
334 the readout ASICs, named Hardroc2 [*Callier, 2014; Seguin-Moreau, 2009*]. The ASICs  
335 dispose of three independent comparators that provide amplitude information about the  
336 registered signals; they also timestamp the signals using a 5 MHz clock. The GRPCs  
337 are operated in avalanche mode, with the high voltage (typically 7 kV) being adapted

continuously to environmental pressure and temperature conditions in order to ensure a stable working point both in terms of detection efficiency and dark noise.

The chambers and their readout electronics are placed in aluminium cassettes for protection while also simplifying greatly the handling of the detector: they are  $361 \times 746 \text{ mm}^2$  large, 31 mm thick, weigh 6 kg each and are transported in a standard foam packaging. Each detection layer, about  $1 \text{ m}^2$  large, consists of 6 cassettes inserted in a light aluminium structure. The separation between the layers is 33 cm, amounting to a total lateral extension of the telescope of 1 m. Low and high voltage are distributed to transfer boxes attached to each layer and further routed to the detector through cabling internal to the aluminium frame. Similarly, the gas distribution is chained through the individual chambers with a unique inlet and outlet per layer. This way, mounting and dismantling of the detector is greatly simplified.

A dedicated board on each detection unit, the DIF [*Adloff*, 2013], using Field Programmable Gate Arrays (FPGAs) serves as an interface between its PCB and the master clock on one side and the acquisition computer on the other side. The synopsis of the data acquisition is as follows: each ASIC reads out 64 pads and stores up to 128 events (an event is at least one signal in one of the 64 pads read by the ASIC with an amplitude above a predefined threshold) in its internal memory. Once an ASIC fills its memory it sends out a readout request; the DIF board listens continuously for readout requests originating from the 24 ASICs on its attached detector unit and forwards the requests to the master clock board. When the master clock receives a readout request from one of the 24 DIFs of the detector, it stops the acquisition and triggers the readout of the entire detector, in parallel for all the DIFs and serialised to the detector unit level. After

361 the data from the memory of the last ASIC in the chain are read out, the master clock  
362 enables again the data acquisition and the cycle repeats.

363 To operate the DAQ system, a conventional computer is used to send the commands  
364 to the master clock board and to collect the data from the 24 detection units. The low  
365 dark noise rate ( $\sim 0.3$  Hz/cm<sup>2</sup>) allows for a full readout of the chambers, without imposing  
366 coincident signals among chambers situated in different layers. It is possible to filter the  
367 data on the acquisition computer such that only coincident hits in two or three of the four  
368 layers are kept. Conversely, if necessary for detailed detector studies, the entire data can  
369 be recorded.

### 3.1. The Puy de Dôme measurement campaign

370 From beginning of November 2013 to middle of January 2014, the TOMUVOL detector  
371 was deployed in a ground-level building with a very light metallic structure. It was  
372 powered from a standard electrical outlet and remotely controlled using a small radio-  
373 antenna transmitting the data to a powerful antenna situated at the summit of the volcano  
374 operated by the Puy de Dôme Observatory [*OPGC*].

375 The total data taking duration was of 41 days, out of which 7 days were dedicated  
376 in the beginning to detector calibration. The data taking was stopped from December  
377 25th to January 8th. During the data taking the efficiency of individual GRPCs has been  
378 estimated on a per run basis, a run being arbitrarily chosen to last 12h. Similarly the  
379 detection dead time (the time duration when the GRPCs are read out and hence tracks  
380 passing through them are not recorded) is measured on a per run basis, though stability  
381 checks were performed frequently during the run. Overall, the mean value of the chamber

382 detection efficiency over the 24 GRPCs was of  $\sim 95\%$ . The dead time during the stable  
 383 runs was  $6.0 \pm 1.1 \%$ , with an average value of  $7 \%$  over the whole data taking period.

384 The track reconstruction uses only events with coincident hits in all four layers of the  
 385 detector. The measured coincidence rate was  $3.5 \pm 0.1$  Hz.

### 3.2. Data reconstruction

386 The reconstruction algorithm preselects coincident hits in a 200 ns time window in  
 387 at least three of the four detection layers, from which tracks are obtained analytically  
 388 through a straight line minimisation procedure, which allows for track bundles. The  
 389 overall  $\chi^2$ -distribution of the track residuals agrees well with the expectation both in the  
 390 case of 3-layer tracks ( $\chi^2$  distribution with two degrees of freedom) and of 4-layer tracks  
 391 ( $\chi^2$  with four degrees of freedom). In the following, the 3-layer and the 4-layer tracks with  
 392  $\chi^2/ndf \leq 5$  are called “reconstructed tracks”. Even though only the high quality 4-layer  
 393 tracks are used in the analysis, the 3-layer tracks allow us to monitor in real time the  
 394 efficiency of the GRPCs and the overall acceptance. Among the 4-layer tracks, only fully  
 395 isolated tracks, i.e. without any signal recorded in the detector that cannot be directly  
 396 linked to the track, are selected.

397 The background, as defined in Section 1, is further reduced in the final sample with  
 398 respect to the well reconstructed tracks by requiring the tracks to have a  $\chi^2/n.d.f \leq 0.8$ .

399 This tight  $\chi^2/n.d.f$  selection is imposed by the optimisation of the measurement sensi-  
 400 tivity that in turn requires minimising the background flux.

401 It is interesting to notice in Figure 6 that if the selection efficiency, defined as the ratio  
 402 between the number of selected tracks and the number of 4-layer, reconstructed tracks,  
 403 is almost  $65 \%$  for the free sky tracks, it drops to  $30 \%$  in the case of the tracks pointing

404 towards Puy de Dôme. This hints at a significant difference in the population of tracks  
 405 pointing towards the volcano and towards the free sky, respectively.

406 As in the case of the MU-RAY collaboration, the selected tracks are called in the  
 407 following “golden tracks” and their rate as a function of time over the whole data taking  
 408 period is shown in Figure 7. The measured mean value is  $1.64 \pm 0.08$  Hz. A total of  
 409 4.95 million of golden tracks were registered, out of which 1.45 million served for cross-  
 410 checks and 3.5 million were used in the analysis. The background rate is also stable over  
 411 the 34 days of data taking with a mean of  $0.93 \pm 0.11$  mHz, that is more than a factor of  
 412 60 larger than the expected signal from high energy muons crossing the control region.

413 The golden tracks sample shows  $X$  and  $Y$  residuals with means close to 0 and a standard  
 414 deviation better than 1.5 mm, proving that the chambers were sufficiently aligned by  
 415 construction, without any additional measurements on site.

416 The full statistics of golden tracks pointing towards the Puy de Dôme is represented in  
 417 Figure 8 as a function of the elevation angle  $\alpha$  and azimuth  $\beta$ . The volcano topographical  
 418 shape is superimposed in black and it is in an excellent agreement with the volcano  
 419 shadow, as inferred from the depletion in the number of muons.

## 4. Muon flux measurement

### 4.1. Methodology

A useful quantity for characterising the behaviour of a detector meant for measuring a flux of particles is the effective surface,  $S_{eff}$ , which takes into account the detection performance ( $\epsilon$ ) and the geometrical acceptance of the detection setup ( $\mathcal{A}$ ). The detection performance  $\epsilon(\alpha, \beta, p)$  includes the changes in detection, reconstruction and selection efficiency with the momentum  $p$  of the incoming particle and its direction of incidence on

the detector, given by the angles  $\alpha$  and  $\beta$ :

$$\mathcal{S}_{eff}(\alpha, \beta, p) = S_{detector} \cdot \mathcal{A}(\alpha, \beta) \cdot \epsilon(\alpha, \beta, p) \quad (1)$$

420 Only the detector area orthogonal to the incident direction of the particle is effective for  
 421 the detection. Moreover, in the case of the muon telescopes made of parallel layers of  
 422 finite dimensions, the particles are required to physically cross the outer layers in order  
 423 to induce coincident signals. This factor, generally known in the literature as geometrical  
 424 acceptance or geometrical factor, can be analytically calculated for a perfect telescope  
 425 with square layers of size  $l^2$  and a distance  $d$  between the two outermost layers as

$$\mathcal{A}(\alpha, \beta) = \cos \alpha \cdot \cos \beta \cdot \sup \left( 0, 1 - \frac{d \cdot \text{abs}(\tan \beta)}{l} \right) \cdot \sup \left( 0, 1 - \frac{d \cdot \text{abs}(\tan \alpha)}{l \cos \beta} \right)$$

426 with  $\sup(0, x)$  being  $x$  for positive  $x$ , 0 otherwise. In practice, the behaviour of the  
 427 instrument will deviate from the ideal form due to missing or inactive detector parts,  
 428 but they are easily accounted for using ray-tracing simulations.

For a telescope of known effective surface, the number of expected muons as a function of the acquisition time can be directly evaluated by convoluting the effective surface with the differential muon flux  $\Phi(\alpha, \beta, p)$  expected along the direction  $(\alpha, \beta)$ :

$$\mathcal{N}(\alpha, \beta) = \Delta T \cdot \int_{p_{th}}^{\infty} \mathcal{S}_{eff}(\alpha, \beta, p) \cdot \Phi(\alpha, \beta, p) dp \quad (2)$$

429 Here,  $p_{th}$  is the detection threshold on the muon momentum and  $\Delta T$  the acquisition time.

430 The effective surfaces estimated for the two detectors are presented in the following  
 431 under the assumption that  $\epsilon(\alpha, \beta, p)$  is discrete: zero below the momentum threshold  
 432 and independent of the muon momentum above. It is a reasonable assumption when



433 taking into account the amount of matter present in the two detectors that should set the  
 434 threshold in the hundreds of MeV/c - 1 GeV/c range.

435 The scintillators on which the MU-RAY detector is based are stable in time.

436 MU-RAY estimated therefore an average trigger efficiency  $\epsilon_{trig}$  equal to 80% and effi-  
 437 ciency due to the acquisition dead-time  $\epsilon_{dt}$  equal to 80% from measurements performed  
 438 in laboratory before the data taking campaign.

The final efficiency  $\epsilon(\alpha, \beta)$  of Equation 1 can be estimated from the average efficiency due to the analysis cuts, the trigger efficiency and the dead-time efficiency:

$$\epsilon(\alpha, \beta) = \epsilon_{ana} \cdot \epsilon_{trig} \cdot \epsilon_{dt} = 0.3 \quad (3)$$

439 The relative uncertainty for  $\epsilon(\alpha, \beta)$  is estimated to be about 10%.

440 In the case of the TOMUVOL detector (Figure 9, bottom), all factors affecting the  
 441 effective surface are estimated continuously during data taking, using the registered data.  
 442 Though the acquisition dead time is measured per run basis, the detector stability is such  
 443 that the efficiencies of the individual detector cells were averaged over the whole period of  
 444 data taking. Each cell efficiency is estimated as the ratio of the number of 4-layer tracks  
 445 that gave a signal in that cell to the total number of tracks (be them 3-layer or 4-layer) that  
 446 intersect the cell, then a toy Monte-Carlo simulation is employed to compute the effective  
 447 surface of detection for golden tracks for any incoming direction. The statistical error is  
 448 kept below 0.1% such that the systematics dominate the uncertainties. The total relative  
 449 accuracy on the effective surface is estimated to be better than 7% which is sufficient for  
 450 the present purpose. It allows us to correct for crude inhomogeneities in the golden tracks  
 451 rate arising from detector inhomogeneities.

## 4.2. Results

452 The muon flux as a function of the elevation angle  $\alpha$  and azimuth  $\beta$  is estimated for both  
 453 MU-RAY and TOMUVOL by dividing the number of golden tracks in each  $1 \times 1 \text{ deg}^2$   
 454 angular bin centred on  $(\alpha_i, \beta_i)$  to  $\mathcal{S}_{eff}(\alpha_i, \beta_i)$ . The measured flux, averaged over the  
 455 azimuth bins in the control regions ( $\beta \in (-4^\circ, 16^\circ)$  for MU-RAY and  $\beta \in (-10^\circ, 10^\circ)$   
 456 for TOMUVOL) is represented as a function of the elevation angle  $\alpha$  in Figure 10. The  
 457 expectation assuming a uniform density for the Puy de Dôme between 1 and 2 g/cm<sup>3</sup> is  
 458 also shown as a function of  $\alpha$ , again averaged over  $\beta \in (-4^\circ, 16^\circ)$ .

459 Other than the target density, the computation of the transmitted muon flux relies on  
 460 two additional free parameters: the momentum threshold,  $p_{\min}$ , and a global normalisa-  
 461 tion,  $A$ . Both have been fitted to the backward experimental flux over the elevation range  
 462  $\alpha \in (-30^\circ, -5^\circ)$  and yielded the best fit values  $p_{\min}=100 \text{ MeV}$  (for both experiments)  
 463 and  $A = 1.270 \pm 0.228$  ( $A=1.084 \pm 0.055$ ) for MURAY (TOMUVOL). This means that  
 464 MU-RAY measures a free-sky flux 18% lower than TOMUVOL, but both are within one  
 465 standard deviation from the expectation. In the forward region, however, one clearly sees  
 466 that the measured flux of golden tracks is higher, by 1 to 2 orders of magnitude, than the  
 467 expected muon flux of transmitted high energy muons.

468 Over the fit region, the standard deviation between the best fit flux model and ex-  
 469 perimental data is within 8% for TOMUVOL and 27% for MURAY. It arises both from  
 470 systematical uncertainties in the detector effective surface estimate and the flux model.  
 471 We use this standard deviation as a global estimate of the systematic uncertainties affect-  
 472 ing the remnant fluxes behind rock depths larger than 1000 m:

$$\Phi_{\text{MU-RAY}} = 1.83 \pm 0.50(\text{syst}) \pm 0.07(\text{stat}) \text{m}^{-2} \text{day}^{-1} \text{deg}^{-2} \quad (4)$$

$$\Phi_{\text{TOMUVOL}} = 1.95 \pm 0.16(\textit{syst}) \pm 0.05(\textit{stat})\text{m}^{-2}\text{day}^{-1}\text{deg}^{-2} \quad (5)$$

473 These values roughly correspond to the expected flux of high-energy atmospheric muons  
 474 at 18° elevation, crossing 600 m.w.e (or 240 m of rock with a density of 2.5 g/cm<sup>3</sup>).

475 The flux measurement presented in Figure 10 shows an excellent performance of both de-  
 476 tectors in situ: they measure accurately the expected direct flux of charged particles from  
 477 the atmosphere. The atmospheric muons are largely dominating among these charged  
 478 particles, and consequently this is de facto a measurement of the atmospheric muon flux,  
 479 though simple trackers as ours cannot distinguish the nature of the incoming particles or  
 480 measure their momentum.

481 The situation becomes more complex when measuring the remnant flux behind a vol-  
 482 cano, i.e. the forward region at positive elevations in Figure 10. The soft component of  
 483 the charged-particles spectrum is little to none affected by the presence of the volcano  
 484 since such particles do not traverse the volcano. They arrive on the detector scattered  
 485 from the free sky, since lower the momentum of the particle, larger its scattering is while  
 486 propagating. The high energy, ballistic muons that cross the volcano and whose transmit-  
 487 tance carries the density information, are however greatly diminished by the absorption  
 488 in the rock. As an order of magnitude example, the expected flux in the free sky at an  
 489 elevation of 24° drops by a rough factor of 130 when measuring behind 500 m.w.e at 18°,  
 490 a factor of 800 for 1000 m.w.e at 11° and about 5000 when measuring behind 2000 m.w.e  
 491 at 3° elevation. With increasing rock thickness and decreasing elevation, the importance  
 492 of the background affecting the muographic measurement (the soft component) is increas-  
 493 ing compared to the muographic signal (the ballistic muons) until it becomes dominant.  
 494 As a result, the density inferred from the muographic measurement that assumes that

495 the measured flux is dominated by ballistic muons is increasingly biased towards lower  
496 densities when the measured rock thickness increases, until a non-physical density of the  
497 volcano is reached at some point. This is illustrated in Table 1 where we showed the effect  
498 of this background level on the muographic measurement of different thicknesses of rock.  
499 The density is inferred assuming that the background is not subtracted from a measure-  
500 ment that includes therefore both the expected flux of atmospheric muons transmitted  
501 through the rock and the background. In the particular case of Puy de Dôme, a reliable  
502 measurement down to an elevation of  $10^\circ$  (that corresponds to about 2000 m.w.e) would  
503 require decreasing the background level by a rough factor of 50.

504 Under the assumption that the background is isotropic and detectors similar in perfor-  
505 mance with ours are used, the background measurement given in Equations 4, 5 allows  
506 inferring the feasibility of muographic measurements in different experimental sites. Ob-  
507 viously, if detectors with particle identification and momentum measurement capabilities  
508 are used, the background can be further reduced.

## 5. Discussion and conclusion

509 The measurement of the flux of particles through the base of the Puy de Dôme vol-  
510 cano presented in this article was performed with two independent detectors, which are  
511 precursors of those foreseen by the MU-RAY and TOMUVOL collaboration. The two  
512 measurements are in agreement but are more than one order of magnitude larger than the  
513 flux of high-energy muons expected to cross the Puy de Dôme volcano at low elevation  
514 (less than  $18^\circ$ ).

515 The theoretical uncertainties affecting the differential flux of atmospheric muons [*Gaisser,*  
516 2012] were estimated to be within 30% from discrepancies between the parametrisation

517 used by TOMUVOL [*Chirkin*, 2004], full CORSIKA [*Heck*, 1998; *Knapp*, 2003] simu-  
518 lations and dedicated measurements [*Sanuki*, 2002; *Motoki*, 2003; *Haino*, 2004]. The  
519 free-sky flux measured by TOMUVOL moreover agrees within 10% with the expected  
520 flux normalisation while the angular dependency is also well reproduced. The difference  
521 in the counting rate can be therefore safely linked to a background source independent of  
522 the sought signal from high energy muons.

523 Though the TOMUVOL detector had no absorber, a steel plate 3 cm thick was used for  
524 the MU-RAY detector (Section 2) to suppress the so called soft component of the cosmic  
525 radiation, consisting of electrons, positrons and  $\gamma$ -photons. The electrons, positrons and  
526 photons are expected to shower when crossing the absorber and an electromagnetic shower  
527 can be rejected by requiring a straight track without additional energy deposits around  
528 it. The steel absorber does not stop or significantly scatter muons with kinetic energies  
529 larger than 70 MeV. The fact that the two detectors observe the same level of background  
530 hints at a main source of background that is not the soft component but rather muons  
531 with kinetic energies greater than 70 MeV.

532 In [*Jourde*, 2013], the DIAPHANE collaboration measured also similar background  
533 levels that they attributed to upward-going muons. Since the MU-RAY and TOMUVOL  
534 detectors do not have yet the ns time resolution that would allow them to differentiate  
535 between down-going tracks coming from the volcano and up-going tracks coming from the  
536 opposite direction (free sky), our background flux measurement could also include such a  
537 contribution. This background is necessarily decreasing with the elevation  $\alpha$  and it could  
538 explain the behaviour of our measured background in the proximity of the horizontal

539 plane, below  $2^\circ$  elevation. Above  $2^\circ$ , our measured background nevertheless remains flat  
540 with the elevation angle until  $8^\circ$  and increases significantly with it afterwards.

541 A study published in [Nishiyama, 2014] leads to very similar results to the MU-RAY  
542 and TOMUVOL measurements presented here. That study used two emulsions-based  
543 detectors with different momentum thresholds (0.2 and 2 GeV/c) and demonstrated that  
544 low-energy particles dominate the background population. However, in that study, as  
545 well as in ours, the detectors cannot provide the necessary particle identification in order  
546 to identify unequivocally the background. One possible background source could be low  
547 energy muons that underwent large-angle scattering during their propagation in the air  
548 or in the vicinity of the detector; the background could be also due to the low energy,  
549 electromagnetic or hadronic components of the down-going atmospheric showers. The  
550 important point is however that by choosing an appropriately high momentum threshold  
551 for the detector the background level can in principle be reduced to a level low enough to  
552 allow a reliable imaging of volcanoes.

553 The joint measurement presented here confirms the need of further tools of background  
554 reduction to explore the interior of volcanoes over a rock thickness of half a kilometre  
555 or more. Both collaborations have already foreseen operating detectors with a higher  
556 momentum threshold and time-of-flight measurements.

557 Even though the 2013 data-taking campaign did not lead to an imaging of the Puy  
558 de Dôme inner structure, it is nonetheless the first measurement of the background flux  
559 behind 1000 m of rock made with two independent detectors situated farther than 1.3 km  
560 away from the volcano. It was found to correspond roughly to the expected flux of high-  
561 energy atmospheric muons at  $18^\circ$  elevation after crossing 600 m.w.e. Though the detection

562 views were South-North for the MU-RAY detector and East-West for the TOMUVOL,  
563 the measured background flux by the two detectors is consistent, hinting towards an  
564 independence with respect to the Earth magnetic field, as it would be expected in case of  
565 the soft component of the spectrum with randomised directions through scattering.

566 The background measurement is a first necessary step before a density measurement is  
567 envisaged. Several groups all over the world were funded over the last ten years and the  
568 number of new muographic project is steadily increasing. Quantifying the background  
569 level should help designing the experimental setups for their designed targets. As already  
570 stressed in Section 4 if the background is isotropic and detectors similar in performance  
571 with ours are used, the background measurement given in Equations 4, 5 allows inferring  
572 the feasibility of muographic measurements in different experimental sites.

573 **Acknowledgments.** The TOMUVOL collaboration acknowledges funding from the  
574 University Blaise Pascal of Clermont-Ferrand, CNRS, Région Auvergne, Conseil Général  
575 du Puy-de-Dôme. During the data taking campaign, the TOMUVOL detector was kindly  
576 hosted in a building belonging to TDF Rhône Auvergne, thanks to Luc Lecoeuvre, head  
577 of the TDF Housing Wealth department. The MU-RAY detector was graciously hosted  
578 by M. Framit in his “Gros Manaux” Inn. The LiDAR data used in this study have  
579 been provided through a collective project driven by the Centre Régional Auvergnat de  
580 l’Information Géographique (CRAIG) which has been financially supported by the Conseil  
581 Général du Puy-de-Dôme, the European Funds for Regional Development (FEDER) and  
582 the Blaise Pascal University of Clermont-Ferrand (UBP). Two of the authors of this article  
583 (L. Gailler and A. Portal) were supported by Clervolc Labex program (ANR-10-LABX-  
584 0006). This is Clervol contribution No. 138.

## References

- 585 Brown, S.K., Loughlin, S.C., Sparks, R.S.J., and Vye-Brown et al., 2015. Global volcanic  
 586 hazards and risk: Technical background paper for the UN-ISDR Global Assessment  
 587 Report on Disaster Risk Reduction 2015, *Global Volcano Model and the International*  
 588 *Association of Volcanology and Chemistry of the Earth's Interior*
- 589 Smith, J.G., Dehn, J., Hoblitt, R.P., LaHusen, R.G., Lowenstern, J.B., Moran, S.C.,  
 590 McClelland, L., McGee, K.A., Nathenson, M., Okubo, P.G., Pallister, J.S., Poland,  
 591 M.P., Power, J.A., Schneider, D.J. and Sisson, T.W., 2009. Volcano monitoring. In: R.  
 592 Young and L. Norby (Editors), *Geological Monitoring*. Geological Society of America,  
 593 Boulder, Colorado, 273–305
- 594 Revil, A., Finizola, A., Piscitelli, S., Rizzo, E., Ricci, T., Crespy, A., Angeletti, B., Balasco,  
 595 M., Barde Cabusson, S., Bennati, L., Bolve, A., Byrdina, S., Carzaniga, N., Di Gangi,  
 596 F., Morin, J., Perrone, A., Rossi, M., Roulleau, E. and Suski, B., 2008. Inner structure  
 597 of La Fossa di Vulcano (Vulcano Island, southern Tyrrhenian Sea, Italy) revealed by  
 598 high-resolution electric resistivity tomography coupled with self-potential, temperature,  
 599 and CO<sub>2</sub> diffuse degassing measurements., *J. Geophys. Res.*, **113**, B7
- 600 Li, Y and Oldenburg, D., 1998. 3-D inversion of gravity data, *Geophysics*, **63**, 109119.
- 601 Gailler, L., Lénat, J.-F., Lambert, M., Levieux, G., Villeneuve, N., Froger,  
 602 J.-L., 2009. Gravity structure of Piton de la Fournaise volcano and inferred  
 603 mass transfer during the 2007 crisis, *J. Volcanol. Geotherm. Res.*, **184**, 31–48.  
 604 doi:10.1016/j.jvolgeores.2009.01.024
- 605 Gailler, L. and Lénat, J.-F., 2012. Architecture of La Réunion inferred from geophysical  
 606 data, *Bulletin of Volcanology*, **221-222**, 83–98. doi: 10.1016/j.jvolgeores.2012.01.015



- 607 Lees, J.M., 2007. Seismic tomography of magmatic systems, *J. Vol-*  
608 *canol. Geotherm. Res.*, **167(1-4)**, 37-56
- 609 McGuire, W. J., 1996. Volcano instability: a review of contemporary themes, *Geological*  
610 *Society, London, Special Publications*, **110(1)**, 1-23
- 611 Siebert, L., Glicken, H., Ui, T., 1987. Volcanic hazards from Bezymianny-and Bandai-type  
612 eruptions, *Bulletin of Volcanology*, **49(1)**, 435-459
- 613 Lopez , D. L. and Williams, S.N., Catastrophic volcano collapse: relation to hydrothermal  
614 al teration. 1993, *Science* **260**, 1794-1796
- 615 L.W. Alvarez, J.A. Anderson, F. El Bedwei, J. Burkhard, A. Fakhry, A. Girgis, A. Goneid,  
616 F. Hassan, D. Iverson, G. Lynch, Z. Miligy, A. H.Moussa, M. Sharkawi, L. Yazolino,  
617 1970. Search for hidden chambers in the pyramids, *Science* **167**, 832
- 618 K Nagamine, M Iwasaki, K Shimomura, K Ishida, 1995. Method of probing inner-structure  
619 of geophysical substance with the horizontal cosmic-ray muons and possible application  
620 to volcanic eruption prediction, *Nucl. Instr. Meth. A*, **356**, 585-595
- 621 H. Tanaka, T, Nakano, S. Takahashi, J. Yoshida, K. Niwa, 2007. Development of an emul-  
622 sion imaging system for cosmic-ray muon radiography to explore the internal structure  
623 of a volcano, Mt. Asama, *Nucl. Instr. Meth. A*, **575**, 489-497
- 624 H. K. M. Tanaka, H.Taira, T. Uchida, M. Tanaka, M. Takeo, T. Ohminato, Y. Aoki, R.  
625 Nishitama, D. Shoji, H. Tsuiji, 2010. Three dimensional computational axial tomog-  
626 raphy scan of a volcano with cosmic ray muon radiography, *J. Geophys. Res.*, **115**,  
627 B12332, doi:10.1029/2010JB007677
- 628 H.K.M. Tanaka, H. Miyajima, T. Kusagaya, A.Taketa, T. Uchida, M. Tanaka, 2011. Cos-  
629 mic muon imaging of hidden seismic fault zones: Rainwater permeation into the mechan-

630 ical fractured zones in Itoigawa–Shizuoka Tectonic Line, Japan, *Earth and Planetary*  
631 *Science Letters*, Volume **306**, Issues 3-4, Pages 156-162

632 H.K.M. Tanaka, T. Kusagaya, H. Shinohara, 2014. Radiographic visualization of magma  
633 dynamics in an erupting volcano, *Nature Communications*, DOI: 10.1038/ncomms4381

634 Major, J.J., Dzurisin D., Schilling S.P., Poland M.P., 2009. Monitoring lava-dome growth  
635 during the 2004-2008 Mount St. Helens, Washington, eruption using oblique terrestrial  
636 photography, *Earth Planet. Sci. Lett.*, **286(1-2)**, 243–254

637 Vallance, J. W., Gardner, C., Scott, W. E., Iverson, R., Pierson, T., 2010. Mount St.  
638 Helens: A 30-Year Legacy of Volcanism, *EOS*, **91**, 169–170. doi:10.1029/2010EO190001

639 Swanson, D.A., Dzurisin, D., Holcomb, R.T., Iwatsubo, E.Y., Chadwick, W.W., Jr.,  
640 Casadevall, T.J., Ewert, J.W., Heliker, C.C., 1987. Growth of the lava dome at Mount  
641 St. Helens, Washington (USA), 1981–83, in Fink, J.H., (ed.), Emplacement of silicic  
642 domes and lava flows, *Geological Society of America Special Paper*, **212**, 1–16

643 Nakada, S., and T. Fujii, 1993. Preliminary report on the activity at Unzen Volcano  
644 (Japan), November 1990–November 1991: Dacite lava domes and pyroclastic flows,  
645 *J. Volcanol. Geotherm. Res.*, **54(3-4)**, 319–333 doi:10.1016/0377-0273(93)90070-8.

646 Nakada, S., Y. Miyake, H. Sato, O. Oshima, A. Fujinawa, 1995. Endogenous growth of  
647 dacite dome at Unzen volcano (Japan), 1993–1994, *Geology*, **23(2)**, 157.

648 Nakada, S., H. Shimizu, K. Ohta, 89(1-4). 1-22, *J. Volcanol. Geotherm. Res.*, **1999**,  
649 Overview of the 1990–1995 eruption at Unzen Volcano. doi:10.1016/S0377-  
650 0273(98)00118-8

651 Calder, E. S., R. Lockett, R. S. J. Sparks, B. Voight, 2002. Mechanisms of lava dome  
652 instability and generation of rockfalls and pyroclastic flows at Soufrière Hills Volcano,

- 653 Montserrat, *Mem. Soc. LONDON*, **21**, 173190
- 654 Ryan, G. A., S. C. Loughlin, M. R. James, L. D. Jones, E. S. Calder, T. Christopher,  
655 M. H. Strutt, and G. Wadge, 2010. Growth of the lava dome and extrusion rates at  
656 Soufrière Hills Volcano, Montserrat, West Indies, 2005–2008, *Geophys. Res. Lett.*, **37**,  
657 L00E08. doi:10.1029/2009GL041477
- 658 Watts, R. ., R. A. Herd, R. S. J. Sparks, and S. R. Young, 2002. Growth patterns and  
659 emplacement of the andesitic lava dome at Soufrière Hills Volcano, Montserrat, *Geol.*  
660 *Soc. London, Mem.*, **21(1)**, 115152, doi:10.1144/GSL.MEM.2002.021.01.06.
- 661 Bluth, G. J. S., and W. I. Rose, 2004. Observations of eruptive activity at San-  
662 tiaguito volcano, Guatemala, *J. Volcanol. Geotherm. Res.*, **136(3-4)**, 297–302.  
663 doi:10.1016/j.jvolgeores.2004.06.001.
- 664 Harris, A.J.L., Rose, W.I., Flynn, L.P., 2003. Temporal trends in lava dome extrusion at  
665 Santiaguito, 1922–2000, *Bulletin of Volcanology*, **65**, 77-89
- 666 Rose, W.I., 1972, Santiaguito Volcanic Dome, *Guatemala Geological Society of America*  
667 *Bulletin*, **83**, 1413–1433. doi: 10.1130/0016-7606(1972)83[1413:SVDG]2.0.CO;2
- 668 J. Marteau, D. Gibert, N. Lesparre, F. Nicollin, P. Noli, F. Giacoppo, 2012. Muons  
669 tomography applied to geosciences and volcanology, *Nucl. Instr. Meth. A*, **695**, 23-28
- 670 N. Lesparre, D. Gibert, J. Marteau, J.-C. Komorowski, F. Nicollin, O. Coutant, 2012.  
671 Density muon radiography of La Soufrière of Guadeloupe volcano: comparison with  
672 geological, electrical resistivity and gravity data, *Geophys. J Int.*, **190**, 1008-1019
- 673 F. Fehr, for the Tomuvol Collaboration, 2012. Density imaging of volcanos with atmo-  
674 spheric muons, *J. Phys.: Conf. Ser.* **375** 052019

675 A. Portal, P. Labazuy, J.-F. Lénat, S. Béné, P. Boivin, E. Busato, C. Cârloganu, C.  
676 Combaret, P. Dupieux, F. Fehr, P. Gay, I. Laktineh, D. Miallier, L. Mirabito, V. Niess,  
677 and B. Vulpesu, 2013. Inner structure of the Puy de Dme volcano: cross-comparison of  
678 geophysical models (ERT, gravimetry, muon imaging), *Geosci. Instrum. Method. Data*  
679 *Syst.*, **2**, 47–54

680 F Ambrosino, A Anastasio, D Basta, L Bonechi, M Brianzi, A Bross, S Callier, A Caputo,  
681 R Ciaranfi, L Cimmino, R D’Alessandro, L D’Auria, C de La Taille, S Energico, F  
682 Garufi, F Giudicepietro, A Lauria, G Macedonio, M Martini, V Masone, C Mattone,  
683 M C Montesi, P Noli, M Orazi, G Passeggio, R Peluso, A Pla-Dalmau, L Raux, P  
684 Rubinov, G Saracino, E Scarlini, G Scarpato, G Sekhniaidze, O Starodubtsev, P Strolin,  
685 A Taketa, H K M Tanaka, A Vanzanella, L Viliani *et al.*, 2014. The MU-RAY project:  
686 detector technology and first data from Mt. Vesuvius, *JINST*, **9**, C02029

687 A. Anastasio, F. Ambrosino, D. Basta, L. Bonechi, M. Brianzi, A. Bross, S. Callier,  
688 A. Caputo, R. Ciaranfi, L. Cimmino, R. D’Alessandro, L. D’Auria, C. de La Taille, S.  
689 Energico, F. Garufi, F. Giudicepietro, A. Lauria, G. Macedonio, M. Martini, V. Masone,  
690 C. Mattone *et al.*, 2013. The MU-RAY detector for muon radiography of volcanoes,  
691 *Nucl. Instr. Meth. A*, **732**, 423-426.

692 A. Anastasio, F. Ambrosino, D. Basta, L. Bonechi, M. Brianzi, A. Bross, S. Callier, F.  
693 Cassese, G. Castellini, R. Ciaranfi, L. Cimmino, R. D’Alessandro, B. De Fazio, C. de La  
694 Taille, F. Garufi, G. Iacobucci, M. Martini, V. Masone, C. Mattone, S. Miyamoto, M.C.  
695 Montesi *et al.*, 2013. The MU-RAY experiment. An application of SiPM technology to  
696 the understanding of volcanic phenomena, *Nucl. Instr. Meth. A*, **718**, 134

- 697 G. Ambrosi, F. Ambrosino, R. Battiston, A. Bross, S. Callier, F. Cassese, G. Castellini, R.  
698 Ciaranfi, F. Cozzolino, R. DAlessandro, C. de La Taille, G. Iacobucci, A. Marotta, V.  
699 Masone, M. Martini, R. Nishiyama, P. Noli, M. Orazi, L. Parascandolo, P. Parascandolo,  
700 G. Passeggio *et al.*, 2011. The MU-RAY project: Volcano radiography with cosmic-ray  
701 muons, *Nucl. Instr. Meth. A*, **628**, 120
- 702 C. Cârloganu, V. Niess, S. Béné, E. Busato, P. Dupieux, F. Fehr, P. Gay, D. Miallier, B.  
703 Vulpescu, P. Boivin, C. Combaret, P. Labazuy, I. Laktineh, J.-F. Lénat, L. Mirabito,  
704 A. Portal, 2013. Towards a muon radiography of the Puy de Dôme, *Geosci. Instrum.*  
705 *Method. Data Syst.*, **2**, 55–60
- 706 Boivin P., Thouret J.C., 2013. The volcanic Chaîne des Puys: A unique collection of  
707 simple and compound monogenetic edifices. In *Landscapes and Landforms of France*  
708 (Fort M. and André M.F., eds), Springer, Heidelberg, 9, 81–91
- 709 Camus, G., 1975. La Chaîne des Puys. Etude structurale et volcanologique, *PhD thesis*  
710 no **56**, Clermont II, 322 p
- 711 Miallier, D., Boivin P., Deniel C., Gourgaud A., Lanos P., Sforza M., and Pilleyre T.,  
712 2010, The ultimate summit eruption of Puy de Dôme volcano (Chaîne des Puys, French  
713 Massif Central) about 10,700 years ago, *Comptes Rendus Geosci.*, **342(11)**, 847–854,  
714 doi:10.1016/j.crte.2010.09.004
- 715 Boivin P., Besson J.C., Briot D., Camus G., de Goër de Herve A., Gourgaud A., Labazuy  
716 P., Langlois E., de Larouzière F.D., Livet M., Mergoïl J., Miallier D., Morel J.M., Vernet  
717 G., Vincent P., 2009 Volcanologie de la Chane des Puys, *Parc Naturel Rgional de la*  
718 *Chane des Puys (Edit.)*, 196p

- 719 S. Okubo, H.K.M. Tanaka, 2012. Imaging the density profile of a volcano interior with  
720 cosmic-ray muon radiography combined with classical gravimetry, *Meas. Sci. Technol.*,  
721 **23** 042001, Doi:10.1088/0957-0233/23/4/042001
- 722 S. Matsuno, F. Kajino, Y. Kawashima, T. Kitamura, K. Mitsui, Y. Muraki, Y. Ohashi,  
723 A. Okada, T. Suda, Y. Minorikawa, K. Kobayakawa, Y. Kamiya, I. Nakamura, and T.  
724 Takahashi, 1984. Cosmic-ray muon spectrum up to 20 TeV at 89° zenith angle, *Phys.*  
725 *Rev. D*, **29**, 1
- 726 K.A. Olive et al. (Particle Data Group), 2014. The Review of Particle Physics, *Chin. Phys.*  
727 *C*, **38**, 090001 and <http://pdg.lbl.gov/2014/AtomicNuclearProperties/index.html>
- 728 S. Agostinelli et al (Geant 4 collaboration), 2003. Geant4—a simulation toolkit, *Nucl. In-*  
729 *str. Meth. A*, **506**, 250–303
- 730 D. Chirkin, 2004. Fluxes of Atmospheric Leptons at 600 GeV - 60 TeV, arxiv:hep-  
731 ph/0407078
- 732 D.E. Groom, N.V. Mokhov, and S.I. Striganov, 2001. Muon stopping power and range  
733 tables 10 MeV-100 TeV, *Atomic Data and Nuclear Data Tables* **78**, 183–356
- 734 A. Pla-Dalmau, A. D. Bross, K. L. Mellot, FERMILAB-Conf-99/095
- 735 A. Piazza, M. Boscardin, G.-F. Dalla Betta, A. Del Guerra, M. Melchiorri, C. Piemonte,  
736 A. Tarolli, N. Zorzi, 2010. Characterization and simulation of different SiPM structures  
737 produced at FBK, *Nucl. Instr. Meth. A*, **617**, 417–419
- 738 G. Punzi, Phystat 2003: Sensitivity of Searches for New Signals and Its Optimization,  
739 Scuola Normale Superiore and INFN, Pisa, Italy
- 740 M Bedjidian, K Belkadhi, V Boudry, C Combaret, D Decotigny, E Cortina Gil, C de la  
741 Taille, R Dellanegra, V A Gapienko, G Grenier, C Jauffret, R Kieffer, M -C Fouz, R

- 742 Han, I Laktineh, N Lumb, K Manai, S Mannai, H Mathez, L Mirabito, J Puerta Pelayo,  
743 M Ruan, F Schirra, N Seguin-Moreau, W Tromeur, M Tytgat, M Vander Donckt and N  
744 Zaganidis, 2011. Performance of Glass Resistive Plate Chambers for a high-granularity  
745 semi-digital calorimeter, *JINST*, **6**, P02001, doi:10.1088/1748-0221/6/02/P02001
- 746 T. Behnke (ed.), “The International Linear Collider Technical Design Report - Volume 4:  
747 Detectors” , Jun 26, 2013. 384 pp, CERN-ATS-2013-037, arXiv:1306.6329
- 748 N. Seguin-Moreau, S. Callier, F. Dulucq, C. De La Taille, G. Martin-Chassard, in “Topical  
749 Workshop on Electronics for Particle Physics (TWEPP-09)” proceedings, Sep 2009,  
750 Paris, France. Cern, pp.122-126
- 751 S. Callier, J.-B Cizel, F. Dulucq, C. de La Taille, G. Martin-Chassard, N. Seguin-Moreau  
752 2014. ROC chips for imaging calorimetry at the International Linear Collider, *JINST*, **9**,  
753 C02022
- 754 C. Adloff, J. Blaha, M. Chefdeville, A. Dalmaz, C. Drancourt, A. Espargilire, R. Gaglione,  
755 N. Geffroy, D. Girard, J. Jacquemier, Y. Karyotakis, I. Koletsou, F. Peltier, J. Samarati,  
756 S. Tsigaridas, G. Tsipolitis, G. Vouters, 2013. Construction and test of a  $1 \times 1$  m<sup>2</sup> Mi-  
757 cromegas chamber for sampling hadron calorimetry at future lepton colliders, *Nucl. In-*  
758 *str. Meth. A*, **729**, 90101
- 759 Observatoire de Physique du Globe de Clermont Ferrand, [http://wwwobs.univ-](http://wwwobs.univ-bpclermont.fr/opgc/index.php)  
760 [bpclermont.fr/opgc/index.php](http://wwwobs.univ-bpclermont.fr/opgc/index.php)
- 761 T.K. Gaisser, 2012. Spectrum of cosmic-ray nucleons, kaon production, and  
762 the atmospheric muon charge ratio, *Astropart. Phys.*, **35**, 801–806, DOI:  
763 10.1016/j.astropartphys.2012.02.010

- 764 D. Heck, J. Knapp, J.N. Capdevielle, G. Schatz, T. Thouw, 1998. A Monte Carlo Code  
765 to Simulate Extensive Air Showers, *Forschungszentrum Karlsruhe Report FZKA 6019*
- 766 J. Knapp, D. Heck, S.J. Sciutto, M.T. Dova, and M. Risse, 2003. Extensive Air Shower  
767 Simulations at Highest Energies, *Astropart. Phys.*, **19**, 77
- 768 T Sanuki, M Fujikawa, K Abe, K Anraku, Y Asaoka, H Fuke, S Haino, M Imori, K Izumi,  
769 T Maeno, Y Makida, N Matsui, H Matsumoto, H Matsunaga, M Motoki, J Nishimura,  
770 M Nozaki, S Orito, M Sasaki, Y Shikaze, T Sonoda, et al., 2002. Measurements of  
771 atmospheric muon spectra at mountain altitude, *Phys. Lett. B*, **541**, 234–242 Erratum-  
772 ibid. B581 (2004) 272-273 DOI: 10.1016/S0370-2693(02)02265-7
- 773 M. Motoki, T. Sanuki, S. Orito, K. Abe, K. Anraku, Y. Asaoka, M. Fujikawa, H. Fuke,  
774 S. Haino, M. Imori, K. Izumi, T. Maeno, Y. Makida, N. Matsui, H. Matsumoto, H.  
775 Matsunaga, J. Mitchell, T. Mitsui, A. Moiseev, J. Nishimura, M. Nozaki, J. Ormes,  
776 T. Saeki, M. Sasaki, E.S. Seo, Y. Shikaze, T. Sonoda, R. Streitmatter, J. Suzuki, K.  
777 Tanaka, I. Ueda, J.Z. Wang, N. Yajima, T. Yamagami, A. Yamamoto, Y. Yamamoto, K.  
778 Yamato, T. Yoshida, K. Yoshimura, 2003. Precise measurements of atmospheric muon  
779 fluxes with the BESS spectrometer, *Astropart. Phys.*, **19**, 113-126 DOI: 10.1016/S0927-  
780 6505(02)00195-0
- 781 S. Haino, T. Sanuki, K. Abe, K. Anraku, Y. Asaoka, H. Fuke, M. Imori, A. Itasaki,  
782 T. Maeno, Y. Makida, S. Matsuda, N. Matsui, H. Matsumoto, J.W. Mitchell, A.A.  
783 Moiseev, J. Nishimura, M. Nozaki, S. Orito, J.F. Ormes, M. Sasaki, E.S. Seo, Y. Shikaze,  
784 R.E. Streitmatter, J. Suzuki, Y. Takasugi, K. Tanaka, K. Tanizaki, T. Yamagami, A.  
785 Yamamoto, Y. Yamamoto, K. Yamato, T. Yoshida, K. Yoshimura, 2004. Measurements  
786 of primary and atmospheric cosmic-ray spectra with the BESS-TeV spectrometer, *Phys.*



787 *Lett. B*, **594**, 35.

788 K. Jourde, D. Gibert, J. Marteau, J. De Bremond D'Ars, S. Gardien, C. Girerd, J.-C.

789 Ianigro, D. Carbone, 2013. Experimental detection of upward going cosmic particles and

790 consequences for correction of density radiography of volcanoes, *Geophys. Res. Lett.*, **40**,

791 6334-6339 doi:10.1002/2013GL058357

792 R. Nishiyama, S. Miyamoto, N. Naganawa, 2014. Experimental study of source of back-

793 ground noise in muon radiography using emulsion film detectors, *Geosci. Instrum.*

794 *Method. Data Syst.*, **3**, 29-39 doi:10.5194/gi-3-29-2014

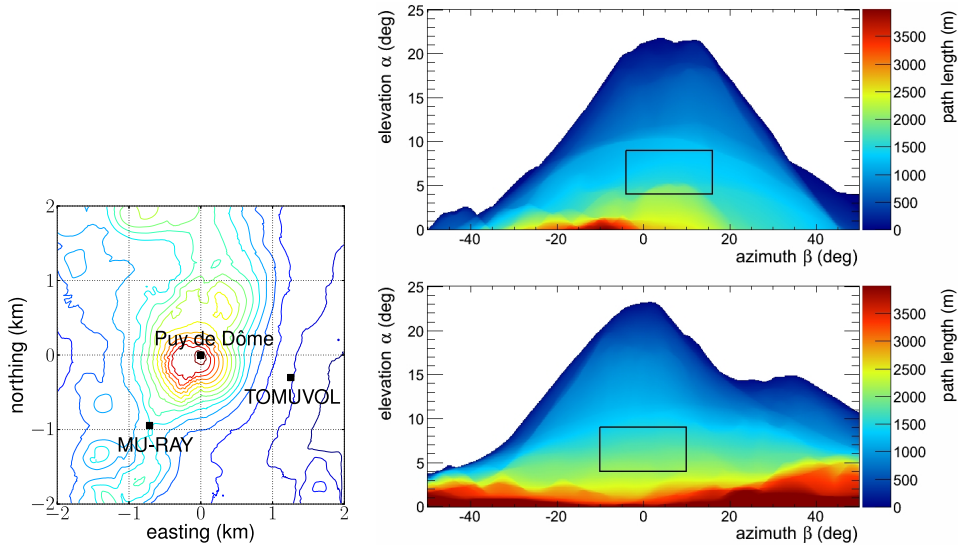


**Figure 1.** *Top:* the deployment sites for the MU-RAY and TOMUVOL detectors on the flank of the Puy de Dôme volcano. The level curves go from 880 m to 1440 m, in 40 m steps. The path length traveled by the atmospheric muons through the volcano before reaching the MU-RAY (*middle plot*) and TOMUVOL (*bottom plot*) detectors, as a function of the elevation angle  $\alpha$  and azimuth  $\beta$ . The control regions, defined by  $\alpha \in (4^\circ, 9^\circ)$  and  $\beta \in (-4^\circ, 16^\circ)$  (MU-RAY) or  $|\beta| \leq 10^\circ$  (TOMUVOL), are indicated by the black rectangles.

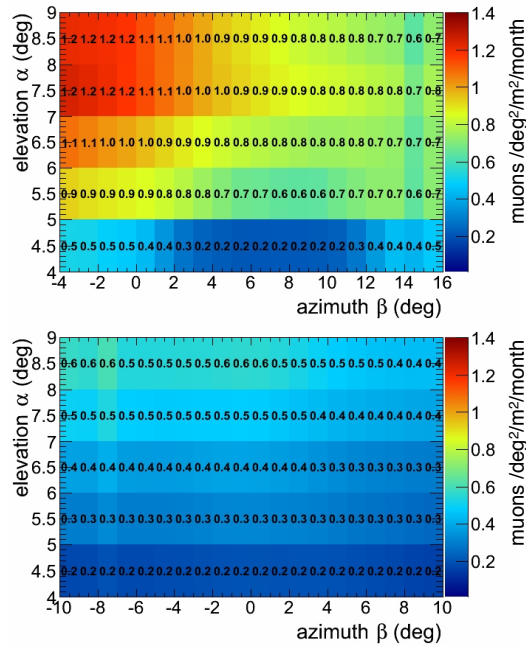


**Figure 2.** Expected number of muons crossing the control regions in a month and measurable with a  $1 \text{ m}^3$ , ideal detector, as a function of the elevation angle  $\alpha$  and azimuth  $\beta$ . The detector is supposed to be fully efficient, with a detection threshold of 100 MeV and is located either at the MU-RAY (*top*) or TOMUVOL (*bottom*) deployment sites. The volcano density is assumed to be  $1.66 \text{ g}/\text{cm}^3$  and uniform.

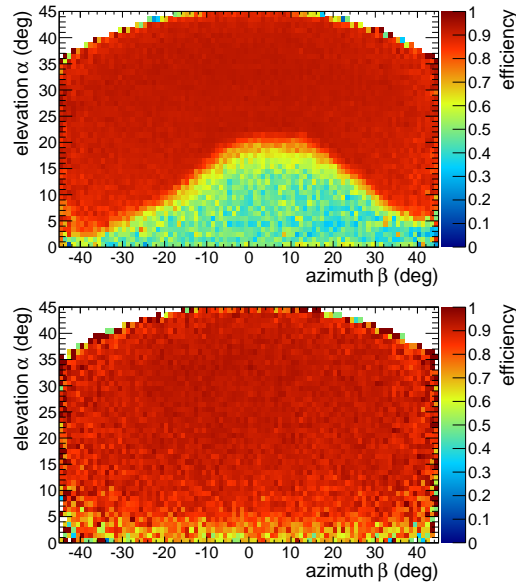


**Figure 3.** MU-RAY selection efficiency for the tracks pointing towards Puy de Dôme (*top*) and in the opposite direction (*bottom*) as a function of the elevation angle  $\alpha$  and azimuth  $\beta$ .

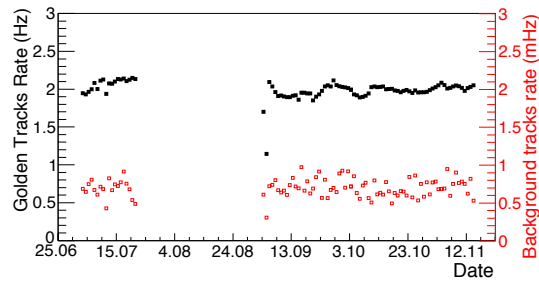


**Figure 4.** Rate of “golden tracks” (black squares, in Hz) and background tracks (open red squares, in mHz), registered with the MU-RAY detector. The rates are corrected for the acquisition dead time.

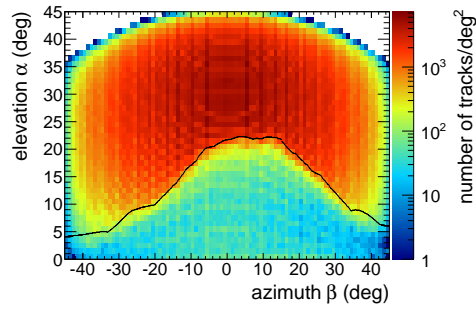


**Figure 5.** MU-RAY golden tracks towards Puy de Dôme as a function of the elevation angle  $\alpha$  and azimuth  $\beta$ . The topographical shape of the Puy de Dôme is superimposed in black.

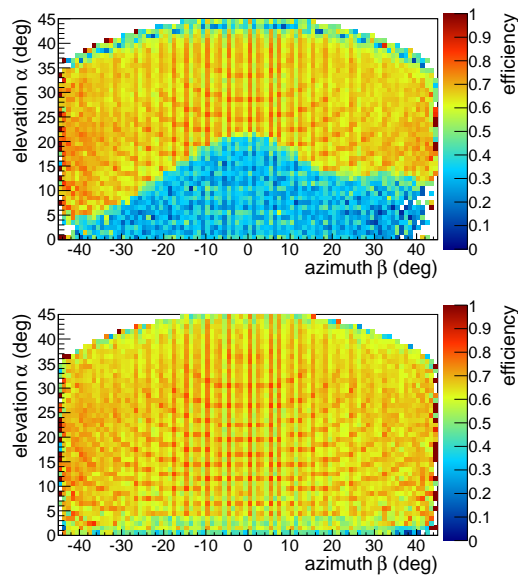


**Figure 6.** Percentage of isolated tracks with  $\chi^2/n.d.f. \leq 0.8$  in the original sample of reconstructed tracks as a function of the elevation  $\alpha$  and azimuth  $\beta$ . *Top* : sample of tracks pointing towards Puy de Dôme; *bottom* : sample of tracks pointing in the opposite direction of Puy de Dôme.

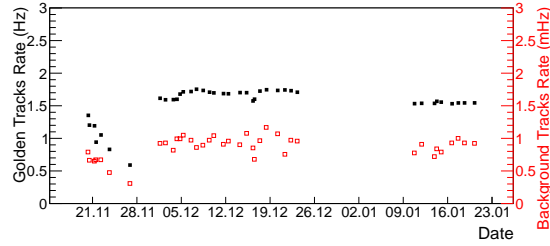


**Figure 7.** Rates of “golden tracks” recorded with the TOMUVOL detector (black squares, in Hz) and background tracks (open red squares, in mHz). The rates are corrected for the acquisition dead time. During the runs before November 28th the detector working conditions (mainly high voltage applied on the GRPCs) were scanned in order to define an optimal working point.

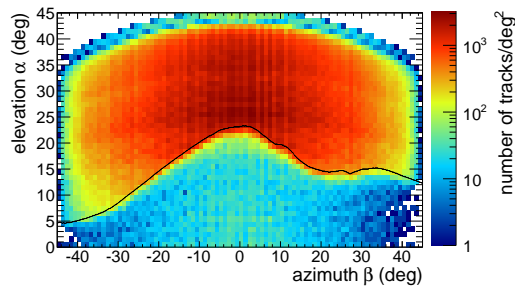


**Figure 8.** Golden tracks recorded by the TOMUVOL detector and pointing towards the Puy de Dôme as a function of the elevation angle  $\alpha$  and azimuth  $\beta$ .

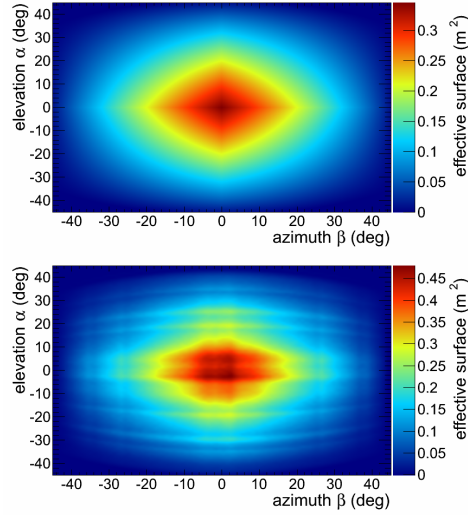


**Figure 9.** Effective surface as a function of the elevation angle  $\alpha$  and azimuth  $\beta$  for MU-RAY (*top*) and TOMUVOL (*bottom*) detectors.

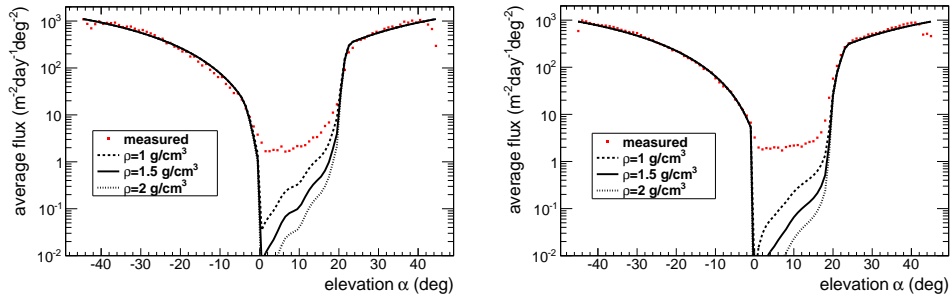


**Figure 10.** Muon flux as a function of the elevation  $\alpha$ , as measured with the MU-RAY (*top*) and TOMUVOL (*bottom*) detectors.

**Table 1.** Transmitted flux of ballistic atmospheric-muons behind different rock thicknesses and the inverted density through a muographic measurement affected by a background flux of  $1.94 \text{ m}^{-2}\text{day}^{-1}\text{deg}^{-2}$  (the quadratic mean of the MU-RAY and TOMUVOL measurements given in Equations 4, 5).

Integrated density (true, mwe)	elevation angle (deg)	transmitted flux ( $\text{m}^{-2}\text{day}^{-1}\text{deg}^{-2}$ )	integrated density (measured, m.w.e)	bias %
500	18	3.18	389.7	-22
1000	11	0.83	539.6	-46
2000	3	0.19	498.3	-75